Ferromagnetism and quantum anomalous Hall effect in one-side-saturated buckled honeycomb lattices

Shin-Ming Huang,[1] Shi-Ting Lee,[1] and Chung-Yu Mou[1,2,3,4]

[1]*Department of Physics, National Tsing Hua University, Hsinchu 30043, Taiwan*

[2]*Frontier Research Center on Fundamental and Applied Sciences of Matters, National Tsing Hua University, Hsinchu 30043, Taiwan*

[3]*Institute of Physics, Academia Sinica, Nankang, Taiwan*

[4]*Physics Division, National Center for Theoretical Sciences, P.O. Box 2-131, Hsinchu, Taiwan*

The recently synthesized silicene as well as theoretically discussed germanene are examples of buckled honeycomb structures. The buckled structures allow one to manipulate asymmetry between two underlying sublattices of honeycomb structures. Here by taking germanene as a prototype of buckled honeycomb lattices, we explore magnetism induced by breaking sublattice symmetry through saturating chemical bonds on one side of the buckled honeycomb lattice. It is shown that when fractions of chemical bonds on one side are saturated, two narrow bands always exist at half filling. Furthermore, the narrow bands generally support flat band ferromagnetism in the presence of the Hubbard U interaction. The induced magnetization is directly related to the saturation fraction and is thus controllable in magnitude through the saturation fraction. Most importantly, we find that depending on the saturation fraction, the ground state of a one-side-saturated germanene may become a quantum anomalous Hall (QAH) insulator characterized by a Chern number that vanishes for larger magnetization. The nonvanishing Chern number for smaller magnetization implies that the associated quantum Hall effect tends to survive at high temperatures. Our findings provide a potential method to engineer buckled honeycomb structures into high-temperature QAH insulators.

I. INTRODUCTION

Since the pioneering work by Kane and Mele in 2005, [1] the quantum spin Hall (QSH) state has gathered great interest in the condensed matter field. The QSH state is characterized by an insulating bulk and gapless helical edge states [2,3]. The original candidate with the QSH effect proposed by Kane and Mele [1] was graphene in which spin-orbit coupling (SOC) opens a gap at the Dirac points and turns the semimetal into a topological insulator. However, SOC in graphene was reported very weak such that QSH effect can be observed only at low temperatures [4,5]. For stronger SOC, heavier elements are possible candidates. Honeycomb lattices formed by other elements of group IV, such as Si and Ge which are termed as silicene and germanene, respectively, are predicted to be stable as planar lattices by first-principles calculations [6–9]. A prominent feature of these materials is the buckled geometry, which allows a tunable band gap via the vertical electric field [10,11]. Although silicene or germanene has not been successfully isolated yet, recent synthesis of silicene through epitaxial growth on silver substrate indicates the feasibility of realizing silicene and germanene [12–14]. It is thus possible that silicene and germanene could follow graphene and open new perspectives for applications, especially due to their compatibility with Si-based electronics.

In addition to the QSH state, another interesting state in graphene-related materials that has been proposed theoretically is the quantum anomalous Hall (QAH) state [15–19]. Similar to the quantum Hall state, the QAH state is also an insulating state without time-reversal symmetry and is characterized by quantized Hall conductance $C_n e^2/h$ (C_n, the Chern number) and the presence of chiral edge states. However, unlike the quantum Hall state which originates from quantized Landau levels induced by magnetic fields, the QAH state arises by nontrivial topology of electronic states associated with SOC and internal magnetization [17,18,20–22]. Some proposals of the QAH effect on graphene have been suggested like such as adatoms [23] and proximity [24]. Due to the difficulty in controlling magnetization and SOC, the QAH effect has not been observed experimentally until very recently, when it has been realized in a magnetically doped topological insulator of Cr-doped $(Bi,Sb)_2Te_3$ [25], where the $C_n = 1$ Hall conductance has been observed in low temperatures around hundreds of mK. The realization of the QAH states has revived hopes for using dissipationless edge states to develop low-power-consumption electronics. However, from fundamental and practical points of view, QAH states with larger band gaps and larger Chern numbers [26–29] have the advantage of a lower contact resistance and possible applications at higher temperatures. Therefore, it is desirable to search for QAH insulators with larger Chern numbers and larger band gaps [26–29].

In this paper, we explore QAH effects driven by spontaneous ferromagnetic (FM) order induced by the Hubbard U interaction in a buckled honeycomb. While our theory and results apply to silicene as well, we shall take germanene as a prototype of buckled honeycomb lattices due to its larger spin-orbit coupling. We show that instead of doping the system using magnetic atoms [25], magnetism can be spontaneously induced by breaking sublattice symmetry through saturating chemical bonds on one side of the buckled honeycomb lattice. One of the ways to saturate the chemical bonds is to hydrogenate silicene or germanene [30]. Ferromagnetism in semihydrogenated honeycomb structures has been reported by means of first-principles calculations for graphene [31] and silicene [32]. In our work, we find that saturation of chemical bonds generally tends to localize electrons and results in flat bands. Furthermore, in the presence of the Hubbard U

interaction, spontaneous ferromagnetism is generally induced in the flat bands. The flat band ferromagnetism for the QAH effect is studied on the dice lattice [33] and a decorated lattice [34]. Here we investigate the QAH effect in flat bands of a one-side-saturated buckled honeycomb lattice for different saturation fractions characterized by $1/q$ with q being an integer. For $q = 1, 2, \ldots, 6$, we find that the critical U for ferromagnetism increases with increasing q. The induced magnetization is directly related to the saturation fraction and is thus controllable in magnitude through the saturation fraction. Furthermore, we find that QAH states with $C_n = -1$ or 2 can be realized among these saturation fractions. Specifically, the band gap of the system is given by the difference of the intrinsic SOC (λ_{SO}) and the FM gap (Δ_{FM}). For smaller magnetization, $\Delta_{\text{FM}} < \lambda_{SO}$ and the Chern number is nonzero. As a result, the Chern number C_n starts from -1 for a smaller magnetization and becomes 0 when the magnetization is large enough (a $C_n = 2$ phase precedes the $C_n = -1$ phase in the 1/4-vacancy system). The nonvanishing Chern number for smaller magnetization implies that the associated QAH effect tends to survive at high temperatures. Our findings thus provide a potential method to engineer buckled honeycomb structures into high-temperature QAH insulators.

This paper is organized as follows. In Sec. II, we present the theoretical model of partially saturated germanene (or silicene) with electron-electron interactions. Here the saturation of chemical bonds is modeled as on-site impurity potentials on A sites with strength V_A. We will focus on the infinite potential limit so that sites with saturated chemical bonds can be treated as vacancies. Section III is devoted to the case of semisaturation in which all A sites are vacancies. In Sec. IV, we investigate the saturation fraction of A sites being 1/2, 1/3, and 1/4. We summarize our results including those of the 1/5- and 1/6-vacancy systems and give our discussion in Sec. V.

II. THEORETICAL MODEL

We start by modeling silicene and germanene using the Kane-Mele model on a honeycomb lattice. The honeycomb lattice for germanene and silicene is different from that of graphene due to the buckled structure. Two sublattices, labeled A and B, are in different planes shifted by some distance. In the absence of interactions and impurities, the tight-binding model for both germanene and silicene is given by [9,19]

$$H = -t \sum_{\langle i,j \rangle \alpha} c_{i\alpha}^\dagger c_{j\alpha} + i \frac{\lambda_{SO}}{3\sqrt{3}} \sum_{\langle\langle i,j \rangle\rangle \alpha\beta} \nu_{ij} c_{i\alpha}^\dagger (\hat{\sigma}_z)_{\alpha\beta} c_{j\beta}$$
$$- i \frac{2}{3} \lambda_{R2} \sum_{\langle\langle i,j \rangle\rangle \alpha\beta} \mu_i c_{i\alpha}^\dagger \hat{z} \cdot (\hat{\sigma} \times \hat{\mathbf{d}}_{ij})_{\alpha\beta} c_{j\beta}. \quad (1)$$

Here α and β are indices for spin. The first term is the nearest-neighbor hopping (between A and B sites). The second term is the intrinsic SOC with $\nu_{ij} = (2/\sqrt{3})\hat{z} \cdot \hat{\mathbf{d}}_{kj} \times \hat{\mathbf{d}}_{ik} = \pm 1$, where $\hat{\mathbf{d}}_{kj}$ and $\hat{\mathbf{d}}_{ik}$ are two unit vectors connecting j and i. The third term is the next-nearest-neighbor Rashba SOC where μ_i alternates sign between sublattices due to the buckled structure. We will set the primitive lattice constant a as unity and adopt parameters for germanene. Following Liu *et al.*'s parameters, [9,19] we shall neglect the nearest-neighbor Rashba SOC due

to its minute value: $t = 1.3$ eV, $\lambda_{SO} = 43$ meV, and $\lambda_{R2} = 10.7$ meV. In this noninteracting system without external fields, electrons are characterized by massive Dirac spectra at $K = (\frac{4\pi}{3}, 0)$ and $-K$ which give rise to the QSH effect.

To include the electron-electron interaction and characterize saturation of chemical bonds on A sites, additional terms with the on-site potential V_i and the Hubbard U interaction are included as

$$\Delta H = \sum_{i \in A, \alpha} V_i c_{i\alpha}^\dagger c_{i\alpha} + U \sum_i c_{i\uparrow}^\dagger c_{i\uparrow} c_{i\downarrow}^\dagger c_{i\downarrow}. \quad (2)$$

Here site i is assigned a vacancy by setting V_i to infinity if the chemical bond of site i is saturated, otherwise V_i is set to zero. In the mean-field approach, the on-site potential will be renormalized by adding the following term

$$\Delta V = U \sum_i \sum_\alpha (n_i/2 - \alpha m_i) c_{i\alpha}^\dagger c_{i\alpha}, \quad (3)$$

where $n_i = \sum_\alpha \langle c_{i\alpha}^\dagger c_{i\alpha} \rangle$ and $m_i = \frac{1}{2} \sum_\alpha \alpha \langle c_{i\alpha}^\dagger c_{i\alpha} \rangle$ is the magnetic polarization. In the following except specified, units of the energies are in terms of eV.

According to the work by Mielke and Tasaki [35,36], for a system with an isolated flat band or a nearly flat band system, a finite Coulomb interaction may reach the Stoner criterion and generally results in ferromagnetism in the flat band. However, for the p-orbital electronic system, the bandwidth is often too large so that the Coulomb interaction is not strong enough to lift up the high degeneracy of ground states. In the following, we shall show that for a bipartite system, the asymmetry in the two sublattices introduced by removing points in one sublattice can generally induce magnetism. For bipartite lattices without SOC, the induced magnetism results from the difference in number of lattice points in the two sublattices and agrees with the expectation from Lieb's theorem [37]. In the presence of spin-orbit interaction, removing points in one sublattice generally results in a flat band due to suppression of the nearest-neighbor hopping around vacancies. The emergence of an isolated flat band enables the realization of magnetism in germanene and silicene.

III. FULL SATURATION

We start by considering the case in which a uniform potential V_A is applied at all A sites. We will investigate finite potential at the beginning and then focus on infinite potential. In the absence of electron-electron interaction, the Hamiltonian at momentum **k** is given by

$$\mathcal{H} = \frac{V_A}{2}(1 + \hat{\tau}_z) + T_{SO}\hat{\tau}_z\hat{\sigma}_z + (T\hat{\tau}_+ + r\hat{\tau}_z\hat{\sigma}_+ + \text{H.c.}), \quad (4)$$

where $\hat{\tau}$ and $\hat{\sigma}$ are the Pauli matrices in the A-B sublattice space and the spin space, and

$$T = -t\left[e^{ik_y/\sqrt{3}} + 2e^{-ik_y/2\sqrt{3}}\cos\left(\frac{1}{2}k_x\right)\right], \quad (5)$$

$$T_{SO} = \frac{2\lambda_{SO}}{3\sqrt{3}}\left[\sin(k_x) - 2\sin\left(\frac{1}{2}k_x\right)\cos\left(\frac{\sqrt{3}}{2}k_y\right)\right], \quad (6)$$

$$r = -\frac{4}{3}\lambda_{R2}\left\{\sqrt{3}\cos\left(\frac{1}{2}k_x\right)\sin\left(\frac{\sqrt{3}}{2}k_y\right)\right.$$
$$\left. + i\left[\sin(k_x) + \sin\left(\frac{1}{2}k_x\right)\cos\left(\frac{\sqrt{3}}{2}k_y\right)\right]\right\}. \quad (7)$$

The combination of different terms in spin results in an easy axis z' in **k** space so that the Hamiltonian can be rewritten as

$$\mathcal{H} = \frac{V_A}{2} + \left(\frac{V_A}{2} + \sqrt{T_{SO}^2 + |r|^2}\hat{\sigma}_{z'}\right)\hat{\tau}_z + T\hat{\tau}_+ + T^*\hat{\tau}_-. \quad (8)$$

The four energy eigenvalues can be then explicitly found in the large V_A limit as

$$E_\sigma^{U_p/L_o} = \frac{V_A}{2} \pm \sqrt{\left(\frac{V_A}{2} + \sigma\sqrt{T_{SO}^2 + |r|^2}\right)^2 + |T|^2}$$
$$\approx \begin{cases} V_A + \sigma\sqrt{T_{SO}^2 + |r|^2} + \frac{|T|^2}{V_A}, \\ -\sigma\sqrt{T_{SO}^2 + |r|^2} - \frac{|T|^2}{V_A}, \end{cases} \quad (9)$$

where U_p and L_o denote upper and lower bands which are separated by a gap of V_A and each one has two subbands labeled by $\sigma = \pm$. In the limit of large V_A, the bandwidths for the upper (U_p) and lower (L_o) bands are determined by SOC (λ_{SO} and λ_{R2}) instead of the hopping integral t. The minimum of $\sqrt{T_{SO}^2 + |r|^2}$ is zero at Γ and $M = (0, \frac{2\pi}{\sqrt{3}})$ points, at which $|T|^2/V_A$ are $9t^2/V_A$ and t^2/V_A, respectively. Therefore, it is a metal or a semimetal when the chemical potential falls inside the two lower bands. In the FM state with a FM gap $\Delta_{\rm FM}$, the ground state is an insulating state when $2\Delta_{\rm FM} > 8t^2/V_A$.

We first examine the phase diagram for ferromagnetism V_A-U space for the electron concentration $n = n_A + n_B = 1$. In Fig. 1, it is shown that ferromagnetism happens at large U and/or V_A, resulting from a large ratio of interaction to bandwidth. Although both U and V_A drive the system toward the strong-coupling limit, there is a difference between them: infinite V_A does not lead to the flat band limit but to a finite bandwidth limited by SOC (exact value being $2\lambda_{SO}$). Therefore, a finite value of U is required for a FM state. Figure 1 also shows that the moment at B sites (m_B) quickly saturates
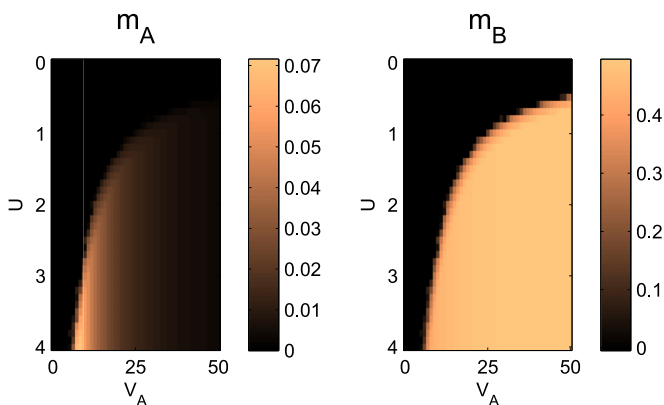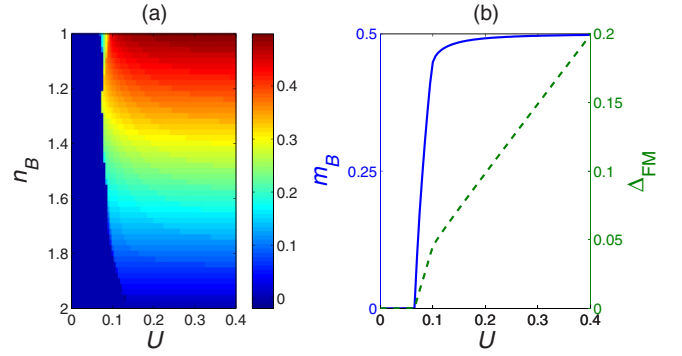

FIG. 2. (Color online) FM moment when all A sites are saturated by infinite V_A. Here the magnetic moment only survives at B sites with $m_B \equiv (n_{B\uparrow} - n_{B\downarrow})/2$. (a) shows the dependence of magnetic momentum on n_B and U, while m_B versus U for $n_B = 1$ is shown in (b) (blue solid line). The FM gap $\Delta_{\rm FM} = Um_B$ is also shown in panel (b) by the green dashed line.

when entering the FM phase, while the moment at A sites (m_A) gradually decreases as V_A increases.

In the following we will focus on the limit $V_A \to \infty$. In this limit, the self-consistent equation for the magnetic moment at the B site is

$$m_B = \frac{1}{N}\sum_{\mathbf{k}} \frac{T_{SO}'(\mathbf{k})}{2E_g(\mathbf{k})}[n_-(\mathbf{k}) - n_+(\mathbf{k})], \quad (10)$$

where $T_{SO}' = T_{SO} + Um_B$, $E_g = \sqrt{(T_{SO}')^2 + |r|^2}$, and $n_\pm = [\exp((\pm E_g - \mu)/kT) + 1]^{-1}$. At zero temperature and $n_B = 1$, the critical U is determined by

$$\frac{1}{U_c} = \frac{1}{N}\sum_{\mathbf{k}} \frac{1}{2E_g^0(\mathbf{k})}, \quad (11)$$

where $E_g^0(\mathbf{k})$ is $E_g(\mathbf{k})$ for $m_B = 0$. T_{SO} in the numerator is absent because its sign oscillates and cancels exactly. In the low-energy region, the Rashba term is linear around Γ and M, $r(\mathbf{k}) \sim \lambda_{R2}(k_y + ik_x)$, while T_{SO} is quadratic around the Γ point and linear around the M point, so a linear dispersion is displayed. As a result, in two dimensions, the critical U is $U_c = c\lambda_{R2}$, where c is a nonuniversal number inversely proportional to the momentum cutoff. In Fig. 2, we show numerical solutions to Eq. (10). The left panel shows the dependence of magnetic moment m_B on n_B and the interaction strength U, while the right panel shows m_B (solid line) and its corresponding gap $\Delta_{\rm FM} \equiv Um_B$ (dashed line) when $n_B = 1$.

Let us elucidate the symmetry of the FM state: the "inversion" symmetry ($\mathbf{k} \to -\mathbf{k}$) is broken, while the threefold rotational symmetry is preserved. Although the lattice has C_6 symmetry, due to SOC, the presence of ferromagnetism breaks the C_6 symmetry and therefore the inversion symmetry is broken. Specifically, a $\pi/3$ rotation of **k** results in $T_{SO}(\mathbf{k}) \to -T_{SO}(\mathbf{k})$ and $r(\mathbf{k}) \to r(\mathbf{k})e^{i\frac{\pi}{3}}$. Therefore, a twofold $\pi/3$ rotation is a $2\pi/3$ rotation that keeps $T_{SO}' = T_{SO} - \Delta_{\rm FM}$ invariant, while a threefold $\pi/3$ rotation is an inversion and cannot keep $T_{SO}' = T_{SO} - \Delta_{\rm FM}$ invariant. As a result, the FM state breaks time-reversal and inversion symmetries and gives rise to odd numbers of Fermi surfaces when it is doped.
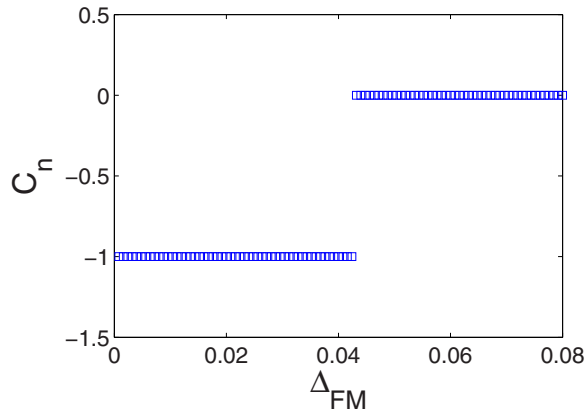

FIG. 1. (Color online) FM moments for finite V_A at A sites (m_A) and B sites (m_B) when $n = n_A + n_B = 1$.

FIG. 3. (Color online) Chern number C_n versus the FM gap Δ_{FM} at $n_B = 1$ when all chemical bonds on A sites are saturated. A topological phase transition occurs at $\Delta_{FM} = \lambda_{SO} = 43$ meV.

In addition, the above symmetry property also requires the FM moment being perpendicular to the x-y plane; otherwise, the C_3 symmetry will be further lost due to the Rashba term.

We turn briefly to the case when the Rashba coupling is turned off. The dominant low-energy dispersion is quadratic now and hence the integral in Eq. (11) gives a logarithmic divergence. Instead of being finite, the critical U becomes zero. Hence the ground state of the system is always FM for any nonvanishing U. In general, for quadratic band crossing, other symmetry breaking might happen [38]. However, for bipartite lattices without SOC, according to Lieb's theorem, finite magnetization is induced by the difference of number of lattice points in the two sublattices. Results based on Eq. (11) thus agree with the expectation of Lieb's theorem.

We now examine the topology of the FM insulating state found in the above. In the limit $V_A \rightarrow \infty$, the Hamiltonian contains only B-site electrons and can be expressed in terms of Pauli matrices $\hat{\sigma}_i$s, $H_\mathbf{k}^B \equiv E_g(\mathbf{k})\hat{d}(\mathbf{k}) \cdot \vec{\sigma}$. By defining $\hat{d}(\mathbf{k}) = (\sin\theta_\mathbf{k}\cos\phi_\mathbf{k}, -\sin\theta_\mathbf{k}\sin\phi_\mathbf{k}, \cos\theta_\mathbf{k})$, the Chern number specifying quantum Hall states can be expressed by

$$C_n = \frac{1}{4\pi}\int d^2\mathbf{k}\,\epsilon_{ij}\partial_{k_i}\cos\theta_\mathbf{k}\partial_{k_j}\phi_\mathbf{k}, \quad (12)$$

which counts the number of field space ($\theta_\mathbf{k}, \phi_\mathbf{k}$) covering a torus in the Brillouin zone (BZ). The nontrivial topological phase is when $\phi_\mathbf{k}$ goes through $[-\pi, \pi]$ and $\theta_\mathbf{k}$ goes through $[0, \pi]$ as $\mathbf{k}$ runs in BZ. Following Fukui and Hatsugai [39], we compute the Chern number numerically. The computed Chern number is shown in Fig. 3. It is seen that the Chern number C_n changes from -1 (QAH insulator) to 0 (a trivial band insulator) as Δ_{FM} increases. The topological phase transition is clearly driven by magnetization. However, unlike the usual transition, nontrivial topology disappears at larger magnetic moments. The topological phase exists when $\max[T'_{SO}(\mathbf{k})] \times \min[T'_{SO}(\mathbf{k})] < 0$; that is, $\Delta_{FM} < \max[T_{SO}(\mathbf{k})] = \lambda_{SO}$. At the critical point $\Delta_{FM} = \lambda_{SO}$, the band gap closes at the K point. Using Fig. 2, one can estimate the criterion on U for the emergence of the QAH insulator. Since larger U implies larger magnetic moment, the results in Fig. 2 imply that U has to lie in the

range 0.07 eV $< U < 0.1$ eV in order to observe the phase of the QAH insulator.

IV. FINITE SATURATION FRACTION

To explore other possible phases, we investigate situations when finite fractions of A sites are saturated. To saturate chemical bonds on part of the A sites, we set V_A to infinity at those A sites. Effectively, vacancies are introduced at those A sites whose chemical bonds are saturated.

In order to systematically investigate finite saturation fractions, we shall consider situations with vacancies arranged in periodic patterns. As a result of including vacancies in periodic patterns, the unit cell changes and becomes a supercell. In the limit of $V_A \rightarrow \infty$, one needs to consider lattice points in a supercell that are not vacancies. Therefore, we shall consider a supercell in which the number of lattice points that excludes vacancies is N_c. After the Fourier transformation, the Hamiltonian in Eq. (1) becomes

$$H = \sum_\mathbf{k} \Psi_\mathbf{k}^\dagger \mathcal{H}_\mathbf{k} \Psi_\mathbf{k}, \quad (13)$$

where $\Psi_\mathbf{k} = (\Psi_\uparrow(\mathbf{k}) \quad \Psi_\downarrow(\mathbf{k}))^t$ with $\Psi_{\sigma=\uparrow,\downarrow}(\mathbf{k})$ being an N_c-component electronic operator, $(c_{1\sigma}(\mathbf{k}), c_{2\sigma}(\mathbf{k}), \ldots, c_{N_c\sigma}(\mathbf{k}))^t$. $\mathcal{H}_\mathbf{k}$ is the Hamiltonian matrix and can be expressed in the following block form:

$$\mathcal{H}_\mathbf{k} = \begin{pmatrix} K_\mathbf{k} + M_\mathbf{k} & \Delta_\mathbf{k} \\ \Delta_\mathbf{k}^\dagger & K_\mathbf{k} - M_\mathbf{k} \end{pmatrix}. \quad (14)$$

Here $K_\mathbf{k}$, $M_\mathbf{k}$, and $\Delta_\mathbf{k}$ are $N_c \times N_c$ matrices. Furthermore, $K_\mathbf{k}$ includes the hopping terms, $M_\mathbf{k}$ includes both the intrinsic SOC and the FM field, and $\Delta_\mathbf{k}$ is the Rashba term.

We first note that there is a chiral symmetry in the matrix $K_\mathbf{k}$. Since there is no on-site energy and hopping only occurs between nearest neighbors (A and B sites), the main diagonal block of $K_\mathbf{k}$ vanishes. Therefore, the unitary matrix U_l that changes $c_A \rightarrow c_A$ and $c_B \rightarrow -c_B$ transforms $K_\mathbf{k}$ into $U_l^\dagger K_\mathbf{k} U_l = -K_\mathbf{k}$. However, since both $M_\mathbf{k}$ and $\Delta_\mathbf{k}$ only couple A sites to A sites or B sites to B sites, the transformation U_l leaves $M_\mathbf{k}$ and $\Delta_\mathbf{k}$ unchanged.

The chiral symmetry of $K_\mathbf{k}$ implies that given an eigenstate of $K_\mathbf{k}$, $|n\rangle$ with energy ε_n, there must be another state $|\bar{n}\rangle \equiv |-n\rangle = U_l|n\rangle$ with negative energy $-\varepsilon_n$. Because $K_\mathbf{k}$ has N_c eigenvalues, if N_c is odd, there will be at least one zero mode for each $K_\mathbf{k}$ block ($\sigma = \uparrow, \downarrow$). Therefore, without including effects due to intrinsic SOC ($M_\mathbf{k}$) and the Rashba interaction ($\Delta_\mathbf{k}$), there are two energy bands which are degenerate at zero energy. We shall denote states of the zero mode by $|0, \mathbf{k}, \sigma = \uparrow, \downarrow\rangle$, if they are the only eigenstates of $K_\mathbf{k}$, and term these two bands as midgap bands. As shown for typical density of states for odd N_c in Fig. 5, the midgap bands persist even if $M_\mathbf{k}$ and $\Delta_\mathbf{k}$ are included.

The emergence of midgap bands is similar to the arising of the impurity bands due to random vacancies in graphene [40]. Without including effects due to intrinsic SOC ($M_\mathbf{k}$) and the Rashba interaction ($\Delta_\mathbf{k}$), two energy bands are degenerate and are composed only by wave functions at B sites. Using $|0, \mathbf{k}, \sigma = \uparrow, \downarrow\rangle$, the effective Hamiltonian for midgap bands that include $M_\mathbf{k}$ and $\Delta_\mathbf{k}$ can be expressed by a simple 2×2
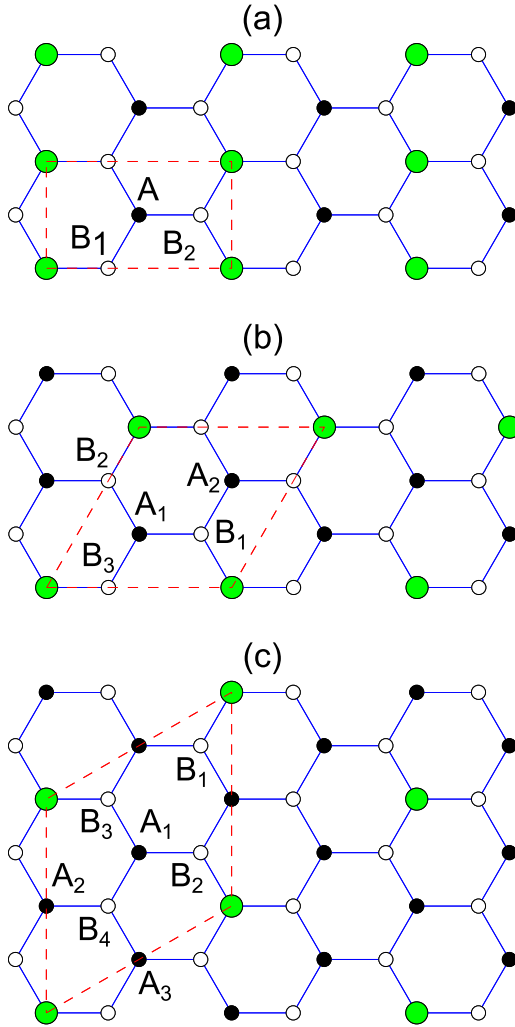
FIG. 4. (Color online) Vacancy arrangements for different vacancy fractions: (a) 1/2 vacancy, (b) 1/3 vacancy, and (c) 1/4 vacancy. Here black circles denote A sites, empty circles denote B sites, and larger green circles denote vacancies. A unit cell (supercell) is enclosed by dashed lines. The horizontal (vertical) direction is taken as the x (y) axis.

matrix

$$H_{\text{mid}}(\mathbf{k}) = \begin{pmatrix} m_{\mathbf{k}} & \delta_{\mathbf{k}} \\ \delta_{\mathbf{k}}^* & -m_{\mathbf{k}} \end{pmatrix}, \tag{15}$$

where $m_{\mathbf{k}} = \langle 0,\mathbf{k},\uparrow|M_{\mathbf{k}}|0,\mathbf{k},\uparrow\rangle$ and $\delta_{\mathbf{k}} = \langle 0,\mathbf{k},\uparrow|M_{\mathbf{k}}|0,\mathbf{k},\downarrow\rangle$. The energy eigenvalues $E_{\text{mid}}^{\pm}(\mathbf{k})$ and eigenstates $|\pm,\mathbf{k}\rangle$ for midgap bands can be estimated by diagonalizing H_{mid} and are given by $E_{\text{mid}}^{\pm}(\mathbf{k}) = \pm E(\mathbf{k})$ with $E(\mathbf{k}) = \sqrt{m_{\mathbf{k}}^2 + |\delta_{\mathbf{k}}|^2}$ and

$$\begin{pmatrix} |+,\mathbf{k}\rangle \\ |-,\mathbf{k}\rangle \end{pmatrix} = \begin{pmatrix} u_{\mathbf{k}} & v_{\mathbf{k}}e^{-i\phi_{\mathbf{k}}} \\ -v_{\mathbf{k}}e^{i\phi_{\mathbf{k}}} & u_{\mathbf{k}} \end{pmatrix} \begin{pmatrix} |0,\mathbf{k},\uparrow\rangle \\ |0,\mathbf{k},\downarrow\rangle \end{pmatrix}, \tag{16}$$

where $u_{\mathbf{k}} = \sqrt{\frac{1}{2}(1 + m_{\mathbf{k}}/E_{\mathbf{k}})}, v_{\mathbf{k}} = \sqrt{\frac{1}{2}(1 - m_{\mathbf{k}}/E_{\mathbf{k}})}$, and $\phi_{\mathbf{k}} = \tan^{-1}(\text{Im } \delta_{\mathbf{k}}/\text{Re } \delta_{\mathbf{k}})$. The magnetic moments in the following cases are found by solving Eq. (10) with E_g being replaced by $E(\mathbf{k})$ and T'_{SO} by $-m_{\mathbf{k}}$.

The vacancy configurations that we shall be focusing on are vacancies arranged in periodic patterns. In general, there are
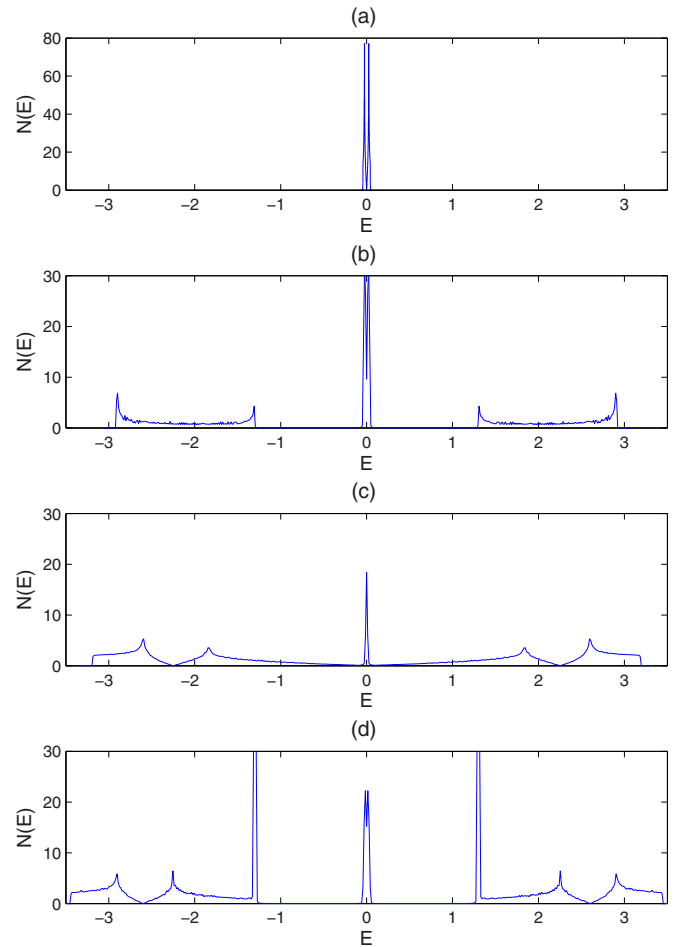

FIG. 5. (Color online) Density of states $N(E)$ for the full saturated system (a), the 1/2-vacancy system (b), the 1/3-vacancy system (c), and the 1/4-vacancy system (d) at $U = 0$ and half filling. The energy E is in units of eV. In addition to midgap bands at center, there are extra side bands: two side bands in (b), four in (c), and six in (d) (here the counting of bands does not include spin degeneracy).

p vacancies in a supercell with the original number of A sites being q. Such configurations are dubbed as a p/q-vacancy system with p, q being mutually prime and $p < q$. In this configuration, a supercell contains $q - p$ A-site and q B-site atoms and hence we have $N_c = 2q - p$ and $2N_c$ bands. For each band in the $2N_c$ bands, the maximal filling is one electron per supercell. Hence there will be maximally one electron in a unit cell belonging to a particular band. However, for the midgap bands, since the wave function is nonvanishing only at B sites, the midgap bands are capable of holding $2/q$ electrons per B site. Hence at half filling, the midgap bands contain $1/q$ electrons per B site. We note that the above argument is based on the assumption that $|0,\mathbf{k},\sigma = \uparrow,\downarrow\rangle$ are the only eigenstates of $K_{\mathbf{k}}$; if not, the midgap states will contain A-site electrons as the 1/3-vacancy case in Sec. IV B.

In this section, we will demonstrate three vacancy fractions: 1/2-, 1/3-, and 1/4-vacancy fractions. The vacancy patterns are illustrated in Fig. 4: (a) for 1/2 vacancy, (b) for 1/3 vacancy, and (c) for 1/4 vacancy. We also calculate 1/5- and 1/6-vacancy cases but to shorten the context we only show their relevant results in the summary, Sec. V.
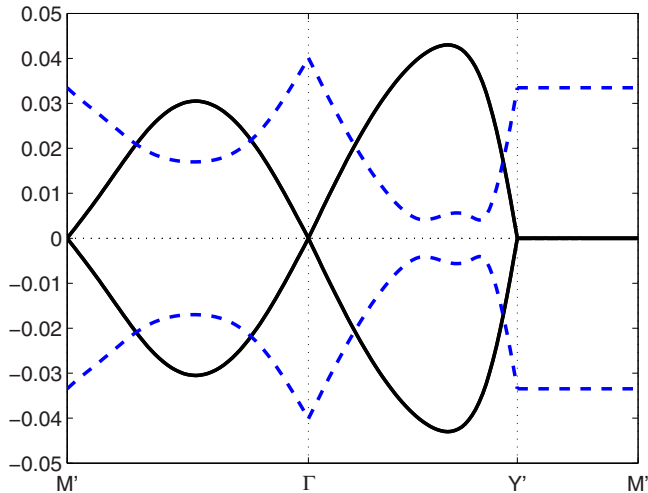
FIG. 6. (Color online) Band structures of the midgap bands in the 1/2-vacancy system: black solid lines for $U = 0$ and dashed lines for $U = 0.18$ eV ($\Delta_{FM} = 38$ meV). Since the inversion symmetry is broken by ferromagnetism, band energies at $\mathbf{k}$ and $-\mathbf{k}$ are different. Here $\mathbf{k}$ is plotted from Γ to $Y' = -(0, \frac{\pi}{a})$ or $M' = -(\frac{\pi}{\sqrt{3}a}, \frac{\pi}{a})$ to exhibit the trend of band touching with increasing Δ_{FM}. The midgap bands touch right at $\mathbf{k} = -(0, \frac{2\pi}{3a})$ when $\Delta_{FM} = \lambda_{SO}$.

A. 1/2 vacancy

The vacancy arrangement for 1/2 vacancy is illustrated in Fig. 4(a), in which a unit cell contains three atoms, A, B_1, and B_2. Detailed band structures are presented in Appendix 1. In Fig. 5(b), we show the density of states when $U = 0$. There are three bands (with twofold degeneracy for each band): a narrow band and two wide bands, separated by gaps about the order of t. As explained before, the midgap bands and their bandwidths are solely determined by the SOC strength. Since λ_{SO} is small, the midgap bands are almost flat and support ferromagnetism. The band structures of the midgap bands are shown in Fig. 6 by the solid lines for $U = 0$ and the dashed lines for $U \neq 0$.

We now examine the FM state in Figs. 7(a) and 7(b). Figure 7(a) shows the density plot of the average moment at B sites $m_B = (m_{B1} + m_{B2})/2$ versus U and the average particle density $n = (n_A + n_{B1} + n_{B2})/3$. It is seen that for moderate magnitude of U, ferromagnetism is always induced. At half filling, the lowest band is completely filled and the chemical potential is right at the center of the midgap band. As a result, the midgap bands make a large contribution to magnetization. This is shown by the solid line in Fig. 7(b). According to the previous elaboration, there is 1/2 electron per B site from each midgap band. Hence the maximal m_B is 1/4, which is in consistent with results shown in Fig. 7(b). Note that in our calculations, a tiny m_A is present due to small deviation of n_A and n_B from one. In Fig. 7(b), we also examine the FM gap Δ_{FM} (the green dashed line) defined by $\Delta_{FM} = U m_B$. Compared with the full-vacancy case in Fig. 2, although m_B saturates quickly also for 1/2 vacancy, both the magnetization and Δ_{FM} are weaker in all doping regimes.

Finally, the topology of the 1/2-vacancy system at half filling is examined by computing the Chern number. We find the same result as in Fig. 3 that the topologically nontrivial state
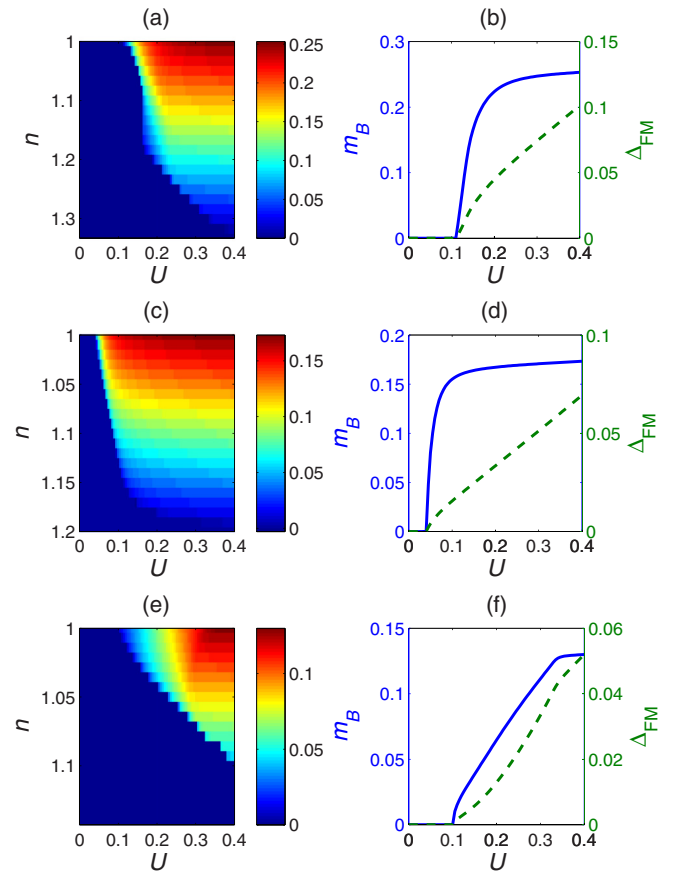

FIG. 7. (Color online) FM moment for the 1/2-vacancy [(a), (b)], 1/3-vacancy [(c), (d)], and 1/4-vacancy [(e), (f)] systems. Left panels (a), (c), and (e) are for average magnetic moment m_B on B sites m_B in the n-U plane. Right panels (b), (d), and (f) show m_B (blue solid lines) and Δ_{FM} (green dashed lines) versus U at $n = 1$. Here $\Delta_{FM} = U m_B$.

($C_n = -1$) exists for $\Delta_{FM} < \lambda_{SO}$. The value of U for $\Delta_{FM} = \lambda_{SO}$ is about 0.195 eV. At the transition point, the midgap bands touch at $\mathbf{k} = (0, -\frac{2\pi}{3a})$, as one can see the tendency from the dashed lines shown in Fig. 6, which is for $\Delta_{FM} = 38$ meV before the transition.

B. 1/3 vacancy

As shown in Fig. 4(b), the unit cell for a 1/3-vacancy lattice contains five atoms, A_1, A_2, B_1, B_2, and B_3. The detail of the bulk band structure is summarized in Appendix 2. The density of states for $U = 0$ is shown in Fig. 5(c). There are five bands with twofold degeneracy for each band. Apparently, there is no large gap opened and the gaps between the midgap bands and its neighbors is λ_{SO}. The band touches in Fig. 5(c) are a numerical artifact. The fact that gaps are of order λ_{SO} instead of t is because there are three zero-energy states of $K_{\mathbf{k}=\Gamma}$. One of three is a state of A-site electrons. As a result, the midgap states when SOC turns on will not contain B-site electrons only. However, we check numerically that the portion of A-site electrons is still tiny. The band structures of the midgap bands are shown in Fig. 8 by the solid lines.

Characterization of the FM states is shown in Figs. 7(c) and 7(d). Due to particular symmetry in the lattice, the spin
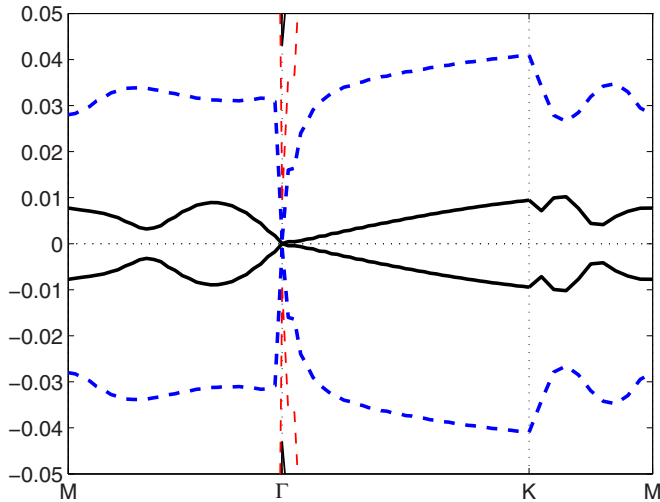
FIG. 8. (Color online) Band structures of midgap bands in the 1/3-vacancy system: black solid lines for $U = 0$ and blue dashed lines for $U = 0.2$ eV ($\Delta_{FM} = 33$ meV). Band edges of two higher-energy bands for $U = 0.2$ eV are also shown by red dashed lines, which move down to zero energy at Γ point when the topological transition occurs.
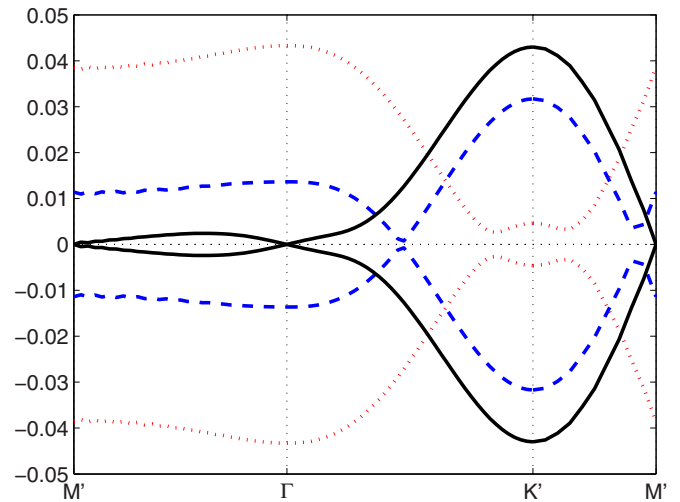

FIG. 9. (Color online) Band structures of the midgap bands in the 1/4-vacancy system: black solid lines for $U = 0$, blue dashed lines for $U = 0.19$ eV ($\Delta_{FM} = 11$ meV), red dotted lines for $U = 0.32$ eV ($\Delta_{FM} = 38$ meV). Note that **k** is plotted from Γ to $K' = -(0, \frac{4\pi}{3c})$ or $M' = -(\frac{\pi}{\sqrt{3}c}, \frac{\pi}{c})$ ($c = 2a$) in order to see the trend of band touching with increasing Δ_{FM}.

(and charge) densities at the A sites and B sites are the same individually. Furthermore, for the same reason as that for the 1/2-vacancy system, there is 1/3 electron per B site from each midgap band. Hence the maximal m_B is 1/6, which is weaker than that of the 1/2-vacancy system. In addition, from the phase diagram in Figs. 7(c) and 7(d), we find that the critical U for emergence of the FM state is smaller than that of the 1/2-vacancy system. This can be understood by the narrow bandwidth in Fig. 8. We show the energy dispersions for $\Delta_{FM} = 33$ meV by the dashed lines in Fig. 8: from the thick dashed lines there is a tiny gap at Γ due to the FM gap from A-site electrons and high-energy bands will move toward zero energy and touch at Γ as indicated by the thin dashed lines.

The topology of the 1/3-vacancy system is examined at half filling. We find the same result as in the cases before that the topologically nontrivial state ($C_n = -1$) exists for $\Delta_{FM} < \lambda_{SO}$. The value of U for $\Delta_{FM} = \lambda_{SO}$ is about 0.255 eV.

C. 1/4 vacancy

Our last example is the 1/4-vacancy system. As shown in Fig. 4(c), the unit cell for the lattice of the 1/4-vacancy system contains three A sites (A_1, A_2, and A_3) and four B sites (B_1, B_2, B_3, and B_4). The detailed band structures are summarized in Appendix 3. In Fig. 5(d), we show the density of states for $U = 0$. It is clear that seven bands with twofold degeneracy for each band can be recognized. The feature of the 1/4-vacancy system is similar to that of the 1/2-vacancy system: there is a large energy gap of order t. Band structures of the midgap bands can be seen in Fig. 9 by the solid lines.

The FM phase diagram is shown in Figs. 7(e) and 7(f). The average moment at the B sites is defined by $m_B = \frac{1}{4}\sum_{i=1}^{4} m_{Bi}$. Due to lattice symmetry, moments at all A sites are the same and moments on B_1, B_2, and B_3 are equal. Figure 7(f) shows

that the critical U at half filling is about 0.1 eV, which is larger than that of the full-vacancy system and is close to that of the 1/2-vacancy system. However, the ferromagnetism is the weakest compared to previous cases: the growth rate of m_B versus U is much slower and the moment is suppressed seriously by doping. The maximal moment will be 1/8 as indicated in Fig. 7(f).

In spite of having weaker ferromagnetism, the 1/4-vacancy system has a nontrivial topology at half filling and may become a QAH insulator in appropriate conditions. Figure 10 shows
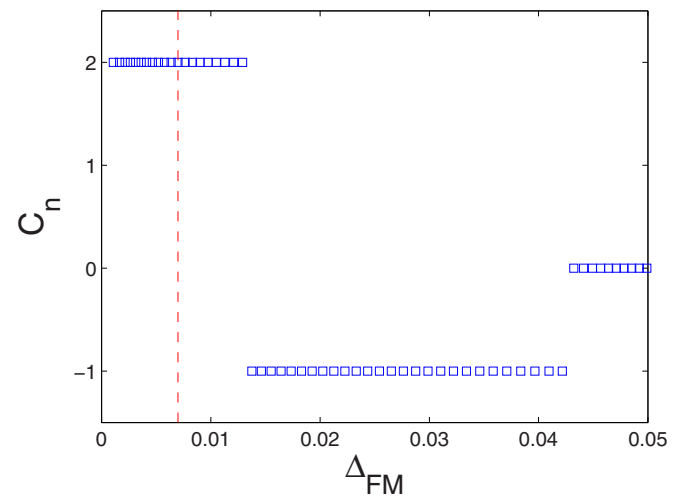

FIG. 10. (Color online) Chern number C_n versus the FM gap Δ_{FM} at $n = 1$ in the 1/4-vacancy system. Two discontinuous transitions are at 13 meV and 43 meV, respectively. Here V_A is set to be ∞. For realistic realization with a finite V_A, the phase boundary of $\Delta_{FM} = 0$ moves to the location of the dashed line so that the region between $\Delta_{FM} = 0$ and the dashed line becomes metallic. Here $V_A = 3t$. See the text, Sec. V, for details.

the computed Chern number at half filling. It is clearly shown that at half filling, the 1/4-vacancy system is a QAH state with $C_n = 2$ when $\Delta_{FM} \lesssim \frac{1}{3}\lambda_{SO}$, a QAH state with $C_n = -1$ when $\frac{1}{3}\lambda_{SO} \lesssim \Delta_{FM} < \lambda_{SO}$, and makes the transition to a trivial insulator when $\Delta_{FM} > \lambda_{SO}$. The transition occurs at the point when two midgap bands touch and the energy gap closes. The band touch occurs when the FM gap exceeds the original gap due to the intrinsic SOC. Hence the criterion of the existence of nontrivial topological phase is $\Delta_{FM} < \lambda_{SO}$. By solving the above condition of band-gap closing for all midgap bands, one finds that the transition occurs when $\Delta_{FM} \approx \frac{1}{3}\lambda_{SO}$ and $\Delta_{FM} = \lambda_{SO}$. The band-touching trends are manifested in Fig. 9: dashed lines for $\Delta_{FM} = 11$ meV and dotted ones for $\Delta_{FM} = 38$ meV. With increasing Δ_{FM}, two bands first touch at the center of $\Gamma K'$ when $\Delta_{FM} \approx \frac{1}{3}\lambda_{SO}$ and then touch at K' when $\Delta_{FM} = \lambda_{SO}$. Detailed demonstrations of the topological transitions are given in Appendix 3.

The topological phases in the 1/4-vacancy system are more feasible than those in the full-vacancy system, in which the QAH state is unrealistic to be implemented due to its narrow phase space. Here, in spite of the same criterion $\Delta_{FM} < \lambda_{SO}$ that has to be satisfied, as shown in Fig. 7(f), the required value of the Hubbard U for Δ_{FM} to reach λ_{SO} is much increased to 0.34 eV as compared to 0.1 eV for the full-vacancy system. The transitions shown in Fig. 10 imply that the QAH phase exists for smaller FM gaps. As the FM gap increases, two midgap bands touch and the topology of the FM states become trivial. Since the FM gap is proportional to the average magnetic moment which decreases in higher temperatures, the results shown in Fig. 10 indicate that the associated QAH effect tends to survive at high temperatures.

V. SUMMARY AND DISCUSSION

In summary, we have investigated ferromagnetism induced by breaking sublattice symmetry through saturating chemical bonds on one side of the buckled honeycomb lattice. The buckled geometry of germanene makes it possible to saturate chemical bonds on one sublattice. It is shown that when fractions of chemical bonds on one side are saturated, two narrow midgap bands always exist at half filling. Furthermore, the midgap bands generally support flat band ferromagnetism in the presence of the Hubbard U interaction. We have shown that given appropriate conditions, midgap bands consist of only B-site electrons (except zero-energy degeneracy in $K_{\mathbf{k}}$) and can be expressed by a spin-1/2 model.

We have considered different concentrations of chemical bonds being saturated by setting the potential to infinity at sites with saturated chemical bonds. Specifically, by considering periodic 1/q-vacancy configurations, the critical interaction for ferromagnetism is highly related to the value of q. In Fig. 11, we summarize the critical U for ferromagnetism for different 1/q-vacancy cases, $q = 1, 2, \ldots, 6$. Two color bars for a given 1/q in Fig. 11 stand for the magnetization reaching 10% (dark one) and 90% (light one) of 1/2q, respectively. As the height difference of two is short, it means a quick magnetic saturation and vice versa. We can see in Fig. 11 that although the critical U for 10% magnetic saturation is nonuniform, the value of U for 90% saturation tends to increase as vacancy concentration decreases (q increases),
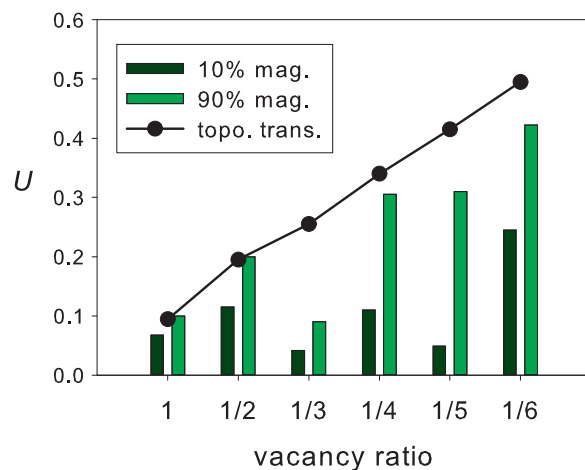

FIG. 11. (Color online) Magnitudes of U (in units of eV) to reach required magnetization in different 1/q-vacancy systems, q from one to six. $q = 1$ is for the full-vacancy system. Green bars are for the U when m_B reaches 10% (dark) and 90% (light) of $1/2 q$, respectively. The filled circles (connected by a solid line) are the values of U making topological phase transitions; i.e., $\Delta_{FM} = \lambda_{SO}$.

except for the 1/3-vacancy system which has a dissimilar band structure.

With ferromagnetism, we find that QAH states can be realized in these six 1/q-vacancy systems and the condition for the QAH phase is $\Delta_{FM} < \lambda_{SO}$. The nontrivial Chern number in these six systems is $C_n = -1$ except that the 1/4-vacancy system has an additional $C_n = 2$ phase for weaker ferromagnetism. The reason why the 1/4-vacancy system can have a larger Chern number is that it doubles the unit length of the vacancy-free system and preserves the C_3 symmetry. Values of U to reach $\Delta_{FM} = \lambda_{SO}$ are also shown by filled circles in Fig. 11. Hence the QAH phase lies in the region below filled circles or the solid line, in which $\Delta_{FM} < \lambda_{SO}$ is satisfied. A linear increase of the critical U for QAH phase is evident. Although a strong interaction leads to large ferromagnetism that tends to break the QAH phase, ferromagnetism becomes weak by decreasing the vacancy ratio and the QAH phase survives in these regimes. In the cases we studied, the critical U increases from 0.1 eV in full-vacancy systems to 0.5 eV in 1/6-vacancy systems. The physical reason why strong ferromagnetism breaks the QAH phase is that in a fully polarized band, the Berry phase due to spins is suppressed. Therefore, in the phase when the Chern number vanishes, the corresponding spin Chern number also vanishes. The QSH phase [19] is thus excluded in our FM models.

In real implementation of saturating chemical bonds, vacancies may not be arranged in a perfect ordered pattern. When vacancies are randomly distributed, the system becomes disordered. Empirically, it is known that disorders generally reduce the coherence of quasiparticles. Hence bandwidths of the midgap bands get broaden. As a result, the density of states drops and ferromagnetism is suppressed [41]. In addition to the broadening of bandwidths, random vacancies generally introduce additional impurity states inside the ferromagnetic gap, which tends to deplete the spectral weight of midgap bands that is responsible for nontrivial Berry phases [42]. As

a result, as the concentration of random vacancies increases, two midgap bands get broadened enough that they eventually merge together with the impurity states. The ferromagnetic gap is destroyed and the QAH effect disappears. Hence a large number of random vacancies is expected to kill the QAH effect in a similar way as disorder kills the QSH effects [42]. Therefore, as long as concentration of random vacancies is kept low ($\leqslant 5\%$) [42], the QAH phase can be realized.

While in our theoretical model the saturation of chemical bonds is modeled by an infinity potential at a given site, in experimental realization such as realization by hydrogenation, the potential at the site with the hydrogen bond is not infinite. Hence for realistic realizations, the saturation of a chemical bond should be modeled by a finite V_A with relevant hopping amplitudes (t') to the saturated site being reduced. For finite potential V_A, an effective hopping of t'^2/V_A between B sites will be induced so that the bandwidth of the impurity band would be larger. This would increase the critical interaction U_c for ferromagnetism to occur. A larger U_c implies a larger FM gap, which is confirmed by the first-principles calculation [32]. However, due to topological robustness of QAH states, we expect that the Berry curvature of the midgap bands and the corresponding Chern number would remain the same. The effects due to finite V_A are examined in Fig. 10. Here we find that for realistic realization with a finite V_A, the phase boundary of $\Delta_{\rm FM} = 0$ moves to the location of the dashed line so that the region between $\Delta_{\rm FM} = 0$ and the dashed line becomes metallic. Here $V_A = 3t$ and $t' = 0.1t$. For smaller $t' = 0.05t$, the metallic phase vanishes. For general finite V_A, in order for the system to be an insulator, the FM gap needs be larger than the bandwidth due to the effective hopping. Hence one requires $\Delta_{\rm FM} > 4t'^2/V_A$. Since the QAH phase requires $\Delta_{\rm FM} < \lambda_{SO}$, it leads to the condition that preserves the QAH phases: $\lambda_{SO} > 4t'^2/V_A$. For typical magnitudes of V_A, we find that when $V_A = 5t$, $t' < 0.2t$ and when $V_A = 3t$, $t' < 0.16t$, which is consistent with results found in Fig. 10. Since conditions on hopping amplitudes found for typical V_A are in the typical range of hopping amplitudes, the above analysis indicates that it is feasible to realize the proposed QAH states by saturating chemical bonds.

In addition to the above-mentioned issue of magnitude of the potential, in real situations, there are also potential complications due to local distortion of the honeycomb lattice. For instance, the appearance of vacancy may modify electronic parameters locally. The perturbation may also lift up the σ bands at Γ [32,43–45], which may change the topology. However, a recent finding shows that hydrogenated graphene actually enhances SOC [46], which can further stabilize the proposed QAH states. It is also shown that by using an appropriate substrate [47], the π bands can be preserved above the σ bands. Although our work does not include all these detailed complications, our results indicate that spontaneous QAH states tend to occur in low concentration limits of vacancies. In low concentrations of vacancies, effects due to local distortions are diluted and one expects that the low-energy physics at half filling is dominated by midgap bands induced by vacancies. Our results thus provide a potential way to engineer buckled honeycomb structures into high-temperature QAH insulators.

APPENDIX: BAND STRUCTURES FOR THE 1/2-, 1/3-, AND 1/4-VACANCY SYSTEMS

1. 1/2 vacancy

According to the lattice shown in Fig. 4(a), the bulk Hamiltonian for the 1/2-vacancy system can be written as $H = H_t + H_{SO} + H_{R2} + H_{FM}$ with

$$H_t = \sum_{\mathbf{k},\sigma} \Psi_\sigma^\dagger(\mathbf{k}) \begin{pmatrix} 0 & \gamma_0(\mathbf{k}) & -t \\ \gamma_0^*(\mathbf{k}) & 0 & 0 \\ -t & 0 & 0 \end{pmatrix} \Psi_\sigma(\mathbf{k}), \quad (A1)$$

$$H_{SO} = \sum_{\mathbf{k},\sigma} \sigma \Psi_\sigma^\dagger(\mathbf{k})$$
$$\times \begin{pmatrix} \gamma_1(\mathbf{k}) & 0 & 0 \\ 0 & -\gamma_1(\mathbf{k}) & f^*(\mathbf{k})\gamma_2(\mathbf{k}) \\ 0 & f(\mathbf{k})\gamma_2(\mathbf{k}) & -\gamma_1(\mathbf{k}) \end{pmatrix} \Psi_\sigma(\mathbf{k}), \quad (A2)$$

$$H_{R2} = \sum_{\mathbf{k}} \Psi_\uparrow^\dagger(\mathbf{k}) \begin{pmatrix} -i\gamma_3(\mathbf{k}) & 0 & 0 \\ 0 & i\gamma_3(\mathbf{k}) & f^*(\mathbf{k})\gamma_4(\mathbf{k}) \\ 0 & f(\mathbf{k})\gamma_4(\mathbf{k}) & i\gamma_3(\mathbf{k}) \end{pmatrix}$$
$$\times \Psi_\downarrow(\mathbf{k}) + \text{H.c.}, \quad (A3)$$

$$H_{FM} = -\sum_{\mathbf{k},\sigma} \sigma \Psi_\sigma^\dagger(\mathbf{k}) \begin{pmatrix} \Delta_A & 0 & 0 \\ 0 & \Delta_{B1} & 0 \\ 0 & 0 & \Delta_{B2} \end{pmatrix} \Psi_\sigma(\mathbf{k}), \quad (A4)$$

where $\Psi_\sigma^\dagger(\mathbf{k}) = (c_{A,\sigma}^\dagger(\mathbf{k}), c_{B1,\sigma}^\dagger(\mathbf{k}), c_{B2,\sigma}^\dagger(\mathbf{k}))$, $\gamma_0(\mathbf{k}) = -2t \cos(\frac{1}{2}k_y a)e^{ik_y a/2}$, $\gamma_1(\mathbf{k}) = \frac{2\lambda_{SO}}{3\sqrt{3}}\sin(k_y a)$, $\gamma_2(\mathbf{k}) = \frac{4\lambda_{SO}}{3\sqrt{3}}\cos(\frac{1}{2}k_x b)\sin(\frac{1}{2}k_y a)$, $\gamma_3(\mathbf{k}) = \frac{4}{3}\lambda_{R2}\sin(k_y a)$, $\gamma_4(\mathbf{k}) = -\frac{4}{3}\lambda_{R2}[\sqrt{3}\sin(\frac{1}{2}k_x b)\cos(\frac{1}{2}k_y a) - i\cos(\frac{1}{2}k_x b)\sin(\frac{1}{2}k_y a)]$, and $f(\mathbf{k}) = e^{ik_x b/2}e^{ik_y a/2}$. The unit length in the x direction is $b = \sqrt{3}a$. FM gaps are defined by $\Delta_A = Um_A$ and $\Delta_{Bi} = Um_{Bi}$ for $i = 1, 2$.

The midgap bands can be constructed explicitly. For the hopping Hamiltonian H_t in Eq. (A1), the eigenstate with eigenvalue zero is given by

$$|0\rangle = \begin{pmatrix} u_1 \\ u_2 \end{pmatrix} = \frac{1}{D} \begin{pmatrix} e^{-ik_y a/2} \\ -2\cos\left(\frac{1}{2}k_y a\right) \end{pmatrix},$$

where D is a normalization factor and is given by $D = \sqrt{1 + 4\cos^2(\frac{1}{2}k_y a)}$. Following Eq. (15), using this basis, the effective Hamiltonian for midgap bands of the 1/2-vacancy system is characterized by expectation values of SOC and the FM field, which are

$$m_{\mathbf{k}} = -\Delta_{B1}|u_1|^2 - \Delta_{B2}|u_2|^2 - \gamma_1 + (W + W^*)\gamma_2,$$
$$\delta_{\mathbf{k}} = i\gamma_3 + (W + W^*)\gamma_4,$$

where $W = f^* u_1^* u_2$.

The topological phase transition occurs at band touching when the corresponding gap closes. At half filling, band

touching occurs between two midgap bands. Therefore, we shall need to find the **k** point(s) at which the gap between two midgap bands closes. In Eq. (15), the gap closes when both $m_\mathbf{k}$ and $\delta_\mathbf{k}$ vanish. It can be identified that the **k** point will be $\mathbf{k} = (0, -\frac{2\pi}{3a})$ at which $\delta_\mathbf{k} = 0$ and at the same time $m_\mathbf{k} = -\frac{1}{2}(\Delta_{B1} + \Delta_{B2}) + \lambda_{SO} = -\Delta_{\mathrm{FM}} + \lambda_{SO}$ (refer to Fig. 6). As the result, the topological phase transition happens at $\Delta_{\mathrm{FM}} = \lambda_{SO}$.

2. 1/3 vacancy

According to the lattice in Fig. 4(b), the bulk Hamiltonian for the 1/3-vacancy system is $H = H_t + H_{SO} + H_{R2} + H_{FM}$ with

$$H_t = -t \sum_{\mathbf{k},\sigma} \Psi_\sigma^\dagger(\mathbf{k}) \begin{pmatrix} 0 & 0 & 1 & 1 & 1 \\ 0 & 0 & 1 & f_1(\mathbf{k}) & f_2(\mathbf{k}) \\ 1 & 1 & 0 & 0 & 0 \\ 1 & f_1^*(\mathbf{k}) & 0 & 0 & 0 \\ 1 & f_2^*(\mathbf{k}) & 0 & 0 & 0 \end{pmatrix} \Psi_\sigma(\mathbf{k}),$$

(A5)

$$H_{SO} = \sum_{\mathbf{k},\sigma} \sigma \Psi_\sigma^\dagger(\mathbf{k}) \begin{pmatrix} M_A(\mathbf{k}) & \mathbf{0}_{2\times3} \\ \mathbf{0}_{3\times2} & M_B(\mathbf{k}) \end{pmatrix} \Psi_\sigma(\mathbf{k}), \quad (A6)$$

$$H_{R2} = \sum_{\mathbf{k}} \Psi_\uparrow^\dagger(\mathbf{k}) \begin{pmatrix} \Delta_A'(\mathbf{k}) & \mathbf{0}_{2\times3} \\ \mathbf{0}_{3\times2} & \Delta_B'(\mathbf{k}) \end{pmatrix} \Psi_\downarrow(\mathbf{k}) + \mathrm{H.c.}, \quad (A7)$$

$$H_{FM} = -\sum_{\mathbf{k},\sigma} \sigma \Psi_\sigma^\dagger(\mathbf{k}) \mathrm{diag} \begin{pmatrix} \Delta_A \\ \Delta_A \\ \Delta_B \\ \Delta_B \\ \Delta_B \end{pmatrix} \Psi_\sigma(\mathbf{k}), \quad (A8)$$

with

$$M_A(\mathbf{k}) = \frac{\lambda_{SO}}{3\sqrt{3}} \begin{pmatrix} 0 & g_0^*(\mathbf{k}) \\ g_0(\mathbf{k}) & 0 \end{pmatrix},$$

$$M_B(\mathbf{k}) = -\frac{\lambda_{SO}}{3\sqrt{3}} \begin{pmatrix} 0 & f_1(\mathbf{k})g_0^*(\mathbf{k}) & g_0(\mathbf{k}) \\ f_1^*(\mathbf{k})g_0(\mathbf{k}) & 0 & f_2(\mathbf{k})g_0^*(\mathbf{k}) \\ g_0^*(\mathbf{k}) & f_2^*(\mathbf{k})g_0(\mathbf{k}) & 0 \end{pmatrix},$$

$$\Delta_A(\mathbf{k}) = \frac{2}{3}\lambda_{R2} \begin{pmatrix} 0 & g_2(\mathbf{k}) \\ g_1(\mathbf{k}) & 0 \end{pmatrix},$$

$$\Delta_B(\mathbf{k}) = -\frac{2}{3}\lambda_{R2} \begin{pmatrix} 0 & f_1(\mathbf{k})g_2(\mathbf{k}) & g_1(\mathbf{k}) \\ f_1^*(\mathbf{k})g_1(\mathbf{k}) & 0 & f_2(\mathbf{k})g_2(\mathbf{k}) \\ g_2(\mathbf{k}) & f_2^*(\mathbf{k})g_1(\mathbf{k}) & 0 \end{pmatrix},$$

where $\Psi_\sigma^\dagger(\mathbf{k}) = (\Psi_{A\sigma}^\dagger(\mathbf{k}), \Psi_{B\sigma}^\dagger(\mathbf{k}))$ with $\Psi_{A\sigma}^\dagger(\mathbf{k}) = (c_{A1,\sigma}^\dagger(\mathbf{k}),$ $c_{A2,\sigma}^\dagger(\mathbf{k}))$ and $\Psi_{B\sigma}^\dagger(\mathbf{k}) = (c_{B1,\sigma}^\dagger(\mathbf{k}), c_{B2,\sigma}^\dagger(\mathbf{k}), c_{B3,\sigma}^\dagger(\mathbf{k}))$. Here the relevant functions are given by $g_0(\mathbf{k}) = i[1 + f_1(\mathbf{k}) + f_2(\mathbf{k})]$, $g_1(\mathbf{k}) = [1 - e^{i\frac{\pi}{3}} f_1(\mathbf{k}) - e^{-i\frac{\pi}{3}} f_2(\mathbf{k})]$, $g_2(\mathbf{k}) = -[1 - e^{i\frac{\pi}{3}} f_1^*(\mathbf{k}) - e^{-i\frac{\pi}{3}} f_2^*(\mathbf{k})]$, and $f_i(\mathbf{k}) = e^{i\mathbf{k}\cdot\vec{b}_i}$ $(i = 1,2)$ for $\vec{b}_1 = b\hat{x}$, $\vec{b}_2 = b(\frac{1}{2}\hat{x} + \frac{\sqrt{3}}{2}\hat{y})$, $\vec{b}_3 = b(\frac{1}{2}\hat{x} - \frac{\sqrt{3}}{2}\hat{y})$ with $b = \sqrt{3}a$. Due to symmetry, FM gaps on two A sites and those on B sites are respectively the same.

For the midgap band, the zero-energy eigenstate $|0\rangle$ of the hopping Hamiltonian H_t in Eq. (A5) is

$$|0\rangle = \begin{pmatrix} u_1 \\ u_2 \\ u_3 \end{pmatrix} = \frac{1}{D} \begin{pmatrix} f_1 - f_2 \\ f_2 - 1 \\ 1 - f_1 \end{pmatrix}$$

with the normalization factor $D = \sqrt{6 - 2\sum_{i=1}^3 \cos \mathbf{k}\cdot\vec{b}_i}$. By using this wave function, $m_\mathbf{k}$ and $\delta_\mathbf{k}$ for the effective Hamiltonian of midgap bands are given by

$$m_\mathbf{k} = -\Delta_{\mathrm{FM}} - [\gamma_{SO} W' + \mathrm{H.c.}],$$
$$\delta_\mathbf{k} = \gamma_1 W' + \gamma_2 W'^*,$$

where $W' = f_1^* u_2^* u_1 + f_2^* u_3^* u_2 + u_1^* u_3$, $\gamma_{SO} = \frac{1}{3\sqrt{3}}\lambda_{SO} g_0$, $\gamma_1 = -\frac{2}{3}\lambda_{R2} g_1$, and $\gamma_2 = \frac{2}{3}\lambda_{R2} g_2$. However, the choice of $|0\rangle$ at Γ is singular, so we have to choose another gauge. This is due to nonuniqueness of the zero-energy eigenstate. At Γ there is degeneracy of three and three wave functions are $\psi_1 = \frac{1}{\sqrt{2}}(1, -1, 0, 0, 0)^t$, $\psi_2 = \frac{1}{\sqrt{6}}(0, 0, 2, -1, -1)^t$, and $\psi_3 = \frac{1}{\sqrt{2}}(0, 0, 0, 1, -1)^t$, respectively. The first one is constructed by A-site electrons while the last two are by B-site electrons. Now the midgap band will contain A-site electrons though a small proportion. This degeneracy explains small gaps (of λ_{SO}) opened between the midgap band and its neighbors in Fig. 5(c).

Finally, we identify the transition point. The band touching occurs at $\mathbf{k} = \Gamma$, where $\Delta_A(\mathbf{k}) = \Delta_B(\mathbf{k}) = 0$ so that spins are decoupled. The effective Hamiltonian of a given spin σ for these three states $\psi_{1,2,3}$ is

$$\mathcal{H}_{\Gamma,\sigma} = -\sigma \begin{pmatrix} \Delta_A & 0 & 0 \\ 0 & \Delta_B & i\lambda_{SO} \\ 0 & -i\lambda_{SO} & \Delta_B \end{pmatrix}.$$

We find that energy eigenvalues are $-\sigma \Delta_A$, $-\sigma(\Delta_B \pm \lambda_{SO})$ and hence the condition for band touching is $\Delta_B = \lambda_{SO}$ (λ_{SO}, $\Delta_B > 0$) as we expect. Here there is a finite (but tiny) Δ_A so that the system is insulating. Note that this tiny Δ_A is present though it is difficult to be identified in Fig. 8.

3. 1/4 vacancy

According to the lattice given by Fig. 4(c), the bulk Hamiltonian for the 1/4-vacancy system is written by $H = H_t + H_{SO} + H_{R2} + H_{FM}$, where

$$H_t = \sum_{\mathbf{k},\sigma} \Psi_\sigma^\dagger(\mathbf{k}) \begin{pmatrix} \mathbf{0}_{3\times3} & T(\mathbf{k}) \\ T^\dagger(\mathbf{k}) & \mathbf{0}_{4\times4} \end{pmatrix} T(\mathbf{k}) \Psi_\sigma(\mathbf{k}), \quad (A9)$$

$$H_{SO} = \sum_{\mathbf{k},\sigma} \sigma \Psi_\sigma^\dagger(\mathbf{k}) \begin{pmatrix} M_A'(\mathbf{k}) & \mathbf{0}_{3\times4} \\ \mathbf{0}_{4\times3} & M_B'(\mathbf{k}) \end{pmatrix} \Psi_\sigma(\mathbf{k}), \quad (A10)$$

$$H_{R2} = \sum_{\mathbf{k},\sigma} \Psi_\uparrow^\dagger(\mathbf{k}) \begin{pmatrix} \Delta_A'(\mathbf{k}) & \mathbf{0}_{3\times4} \\ \mathbf{0}_{4\times3} & \Delta_B'(\mathbf{k}) \end{pmatrix} \Psi_\downarrow(\mathbf{k}) + \mathrm{H.c.}, \quad (A11)$$

$$H_{FM} = -\sum_{\mathbf{k},\sigma} \sigma \Psi_\sigma^\dagger(\mathbf{k}) \text{diag} \begin{pmatrix} \Delta_{A1} \\ \Delta_{A2} \\ \Delta_{A3} \\ \Delta_{B1} \\ \Delta_{B2} \\ \Delta_{B3} \\ \Delta_{B4} \end{pmatrix} \Psi_\sigma(\mathbf{k}), \tag{A12}$$

with

$$T(\mathbf{k}) = -t \begin{pmatrix} 0 & 1 & 1 & 1 \\ f_1'^*(\mathbf{k}) & f_1'^*(\mathbf{k}) & 0 & 1 \\ f_2'^*(\mathbf{k}) & 0 & f_2^*(\mathbf{k}) & 1 \end{pmatrix},$$

$$M_A'(\mathbf{k}) = \frac{1}{3\sqrt{3}}\lambda_{SO} \begin{pmatrix} 0 & -s_1(\mathbf{k}) & s_2(\mathbf{k}) \\ -s_1^*(\mathbf{k}) & 0 & s_3^*(\mathbf{k}) \\ s_2^*(\mathbf{k}) & s_3(\mathbf{k}) & 0 \end{pmatrix},$$

$$\Delta_A'(\mathbf{k}) = \frac{2}{3}\lambda_{R2} \begin{pmatrix} 0 & e^{-i\frac{\pi}{6}}s_1(\mathbf{k}) & -is_2(\mathbf{k}) \\ e^{-i\frac{\pi}{6}}s_1^*(\mathbf{k}) & 0 & e^{i\frac{\pi}{6}}s_3^*(\mathbf{k}) \\ -is_2^*(\mathbf{k}) & e^{i\frac{\pi}{6}}s_3(\mathbf{k}) & 0 \end{pmatrix},$$

and

$$M_B'(\mathbf{k}) = -\frac{1}{3\sqrt{3}}\lambda_{SO} \begin{pmatrix} 0 & s_2(\mathbf{k}) & -s_1(\mathbf{k}) & f_1'(\mathbf{k})s_3^*(\mathbf{k}) \\ s_2^*(\mathbf{k}) & 0 & s_3(\mathbf{k}) & -s_1(\mathbf{k}) \\ -s_1^*(\mathbf{k}) & s_3^*(\mathbf{k}) & 0 & s_2(\mathbf{k}) \\ f_1'^*(\mathbf{k})s_3(\mathbf{k}) & -s_1^*(\mathbf{k}) & s_2^*(\mathbf{k}) & 0 \end{pmatrix},$$

$$\Delta_B'(\mathbf{k}) = -\frac{2}{3}\lambda_{R2} \begin{pmatrix} 0 & -is_2(\mathbf{k}) & e^{-i\frac{\pi}{6}}s_1(\mathbf{k}) & e^{i\frac{\pi}{6}}f_1'(\mathbf{k})s_3^*(\mathbf{k}) \\ -is_2^*(\mathbf{k}) & 0 & e^{i\frac{\pi}{6}}s_3(\mathbf{k}) & e^{-i\frac{\pi}{6}}s_1(\mathbf{k}) \\ e^{-i\frac{\pi}{6}}s_1^*(\mathbf{k}) & e^{i\frac{\pi}{6}}s_3^*(\mathbf{k}) & 0 & -is_2(\mathbf{k}) \\ e^{i\frac{\pi}{6}}f_1'^*(\mathbf{k})s_3(\mathbf{k}) & e^{-i\frac{\pi}{6}}s_1^*(\mathbf{k}) & -is_2^*(\mathbf{k}) & 0 \end{pmatrix}.$$

Here the basis is $\Psi_\sigma^\dagger(\mathbf{k}) = (\Psi_{A\sigma}^\dagger(\mathbf{k}), \Psi_{B\sigma}^\dagger(\mathbf{k}))$ with $\Psi_{A\sigma}^\dagger(\mathbf{k}) = (c_{A1,\sigma}^\dagger(\mathbf{k}), c_{A2,\sigma}^\dagger(\mathbf{k}), c_{A3,\sigma}^\dagger(\mathbf{k}))$ and $\Psi_{B\sigma}^\dagger(\mathbf{k}) = (c_{B1,\sigma}^\dagger(\mathbf{k}), c_{B2,\sigma}^\dagger(\mathbf{k}), c_{B3,\sigma}^\dagger(\mathbf{k}), c_{B4,\sigma}^\dagger(\mathbf{k}))$. Relevant functions are given by $f_i'(\mathbf{k}) = e^{i\mathbf{k}\cdot\vec{c}_i}$ and $s_i(\mathbf{k}) = 2e^{i\mathbf{k}\cdot\vec{c}_i/2}\sin(\frac{1}{2}\mathbf{k}\cdot\vec{c}_i)$ for $i = 1,2,3$. Here $\vec{c}_1 = c(\frac{\sqrt{3}}{2}\hat{x} + \frac{1}{2}\hat{y})$, $\vec{c}_2 = \hat{y}c$, and $\vec{c}_3 = c(\frac{\sqrt{3}}{2}\hat{x} - \frac{1}{2}\hat{y})$ with $c = 2a$. The FM gaps are defined by $\Delta_{Ai} = Um_{Ai}$ $(i = 1,2,3)$ and $\Delta_{Bi} = Um_{Bi}$ $(i = 1,2,3,4)$.

The zero-energy eigenstate $|0\rangle$ of H_t in Eq. (A9) is given by

$$|0\rangle = \begin{pmatrix} u_1 \\ u_2 \\ u_3 \\ u_4 \end{pmatrix} = \frac{1}{D} \begin{pmatrix} 1 - f_1' - f_2' \\ -1 - f_1' + f_2' \\ -1 + f_1' - f_2' \\ 2 \end{pmatrix}$$

with a normalization $D = \sqrt{13 - 2\sum_{i=1}^3 \cos\mathbf{k}\cdot\vec{c}_i}$. Using the wave function as basis, the effective Hamiltonian for the midgap bands are characterized by $m_\mathbf{k}$ and $\delta_\mathbf{k}$, which are given by

$$m_\mathbf{k} = -\sum_{i=1}^4 \Delta_{Bi}|u_i|^2 - \frac{2}{3\sqrt{3}}\lambda_{SO}\text{Re}(W_1 + W_2 + W_3), \quad \delta_\mathbf{k} = -\frac{4}{3}e^{-i\frac{\pi}{6}}\lambda_{R2}\big(\text{Re }W_1 + e^{i\frac{2\pi}{3}}\text{Re }W_2 + e^{i\frac{4\pi}{3}}\text{Re }W_3\big),$$

where $W_1 = -s_1(u_1^*u_3 + u_2^*u_4)$, $W_2 = s_2(u_1^*u_2 + u_3^*u_4)$, $W_3 = s_3(u_2^*u_3 + f_1'^*u_4^*u_1)$.

Finally, we examine the topological phase transitions. The gap closes when both $m_\mathbf{k}$ and $\delta_\mathbf{k}$ vanish. There are twelve points at which $\delta_\mathbf{k} = 0$. These points are Γ, three Ms, $\pm K$, and stars

of $\mathbf{k} = \pm(0, \frac{2\pi}{3c}) \equiv \pm\frac{K}{2}$, respectively [48]. When $\Delta_{FM} = 0$, Γ and Ms are Dirac points. Since at these points Re $W_i = 0$ ($i = 1,2,3$), one gets $m_\mathbf{k} = 0$ when $\Delta_{FM} = 0$. For finite Δ_{FM}, however, gaps are determined by $\pm K = \pm(0, \frac{4\pi}{3c})$ and $\pm\frac{K}{2}$. Hence vanishing of gaps at these points determines the two

topological phase transitions as shown in Fig. 10. Since at $\mathbf{k} = \frac{1}{2}K$ one finds that $m_\mathbf{k} = -\frac{1}{3}(\Delta_{B1} + \Delta_{B2} + \Delta_{B4}) \mp \frac{1}{3}\lambda_{SO} \approx -\Delta_{\text{FM}} \mp \frac{1}{3}\lambda_{SO}$, the first band touch will happen at the star of $-\frac{K}{2}$ when $\Delta_{\text{FM}} \approx \frac{1}{3}\lambda_{SO}$. Moreover, since at $\mathbf{k} = \pm K$ one obtains $m_\mathbf{k} = -\Delta_{\text{FM}} \mp \lambda_{SO}$ ($\Delta_{\text{FM}} = \frac{1}{4}\sum_{i=1}^{4}\Delta_{Bi}$), the second

band touching will happen at $-K$ when $\Delta_{\text{FM}} = \lambda_{SO}$. (Readers can refer to Fig. 9 for the band evolution with Δ_{FM}.) These two bands touch at $\Delta_{\text{FM}} \approx \frac{1}{3}\lambda_{SO}$ and $\Delta_{\text{FM}} = \lambda_{SO}$, which explains the results shown in Fig. 10. In addition, for the first transition because of band touching at three points, the Chern number changes by three, going from $C_n = 2$ to $C_n = -1$.

[1] C. L. Kane and E. J. Mele, Phys. Rev. Lett. **95**, 226801 (2005).

[2] M. Z. Hasan and C. Kane, Rev. Mod. Phys. **82**, 3045 (2010).

[3] M. König, H. Buhmann, L. W. Molenkamp, T. Hughes, C.-X. Liu, X.-L. Qi, and S.-C. Zhang, J. Phys. Soc. Jpn. **77**, 031007 (2008).

[4] H. Min, J. E. Hill, N. A. Sinitsyn, B. R. Sahu, L. Kleinman, and A. H. MacDonald, Phys. Rev. B **74**, 165310 (2006).

[5] Y. Yao, F. Ye, X.-L. Qi, S.-C. Zhang, and Z. Fang, Phys. Rev. B **75**, 041401(R) (2007).

[6] K. Takeda and K. Shiraishi, Phys. Rev. B **50**, 14916 (1994).

[7] S. Cahangirov, M. Topsakal, E. Aktürk, H. Sahin, and S. Ciraci, Phys. Rev. Lett. **102**, 236804 (2009).

[8] C. C. Liu, W. Feng, and Y. Yao, Phys. Rev. Lett. **107**, 076802 (2011).

[9] C. C. Liu, H. Jiang, and Y. Yao, Phys. Rev. B **84**, 195430 (2011).

[10] M. Ezawa, New J. Phys. **14**, 033003 (2012).

[11] Z. Ni, Q. Liu, K. Tang, J. Zheng, J. Zhou, R. Qin, Z. Gao, D. Yu, and J. Lu, Nano Lett. **12**, 113 (2012).

[12] B. Lalmi, H. Oughaddou, H. Enriquez, A. Kara, S. Vizzini, B. Ealet, and B. Aufray, Appl. Phys. Lett. **97**, 223109 (2010).

[13] P. Vogt, P. De Padova, C. Quaresima, J. Avila, E. Frantzeskakis, M. C. Asensio, A. Resta, B. Ealet, and G. LeLay, Phys. Rev. Lett. **108**, 155501 (2012).

[14] C.-L. Lin, R. Arafune, K. Kawahara, N. Tsukahara, E. Minamitani, Y. Kim, N. Takagi, and M. Kawai, Appl. Phys. Express **5**, 045802 (2012).

[15] F. D. M. Haldane, Phys. Rev. Lett. **61**, 2015 (1988).

[16] M. Onoda and N. Nagaosa, Phys. Rev. Lett. **90**, 206601 (2003).

[17] Z. Qiao, S. A. Yang, W. Feng, W.-K. Tse, J. Ding, Y. Yao, J. Wang, and Q. Niu, Phys. Rev. B **82**, 161414(R) (2010).

[18] W. K. Tse, Z. Qiao, Y. Yao, A. H. MacDonald, and Q. Niu, Phys. Rev. B **83**, 155447 (2011).

[19] M. Ezawa, Phys. Rev. Lett. **109**, 055502 (2012).

[20] C.-X. Liu, X.-L. Qi, X. Dai, Z. Fang, and S.-C. Zhang, Phys. Rev. Lett. **101**, 146802 (2008).

[21] C. Wu, Phys. Rev. Lett. **101**, 186807 (2008).

[22] Z. Qiao, H. Jiang, X. Li, Y. Yao, and Q. Niu, Phys. Rev. B **85**, 115439 (2012).

[23] H. Zhang, C. Lazo, S. Blügel, S. Heinze, and Y. Mokrousov, Phys. Rev. Lett. **108**, 056802 (2012).

[24] Z. Qiao, W. Ren, H. Chen, L. Bellaiche, Z. Zhang, A. H. MacDonald, and Q. Niu, Phys. Rev. Lett. **112**, 116404 (2014).

[25] C. Z. Chang *et al.*, Science **340**, 167 (2013).

[26] H. Jiang, Z. Qiao, H. Liu, and Q. Niu, Phys. Rev. B **85**, 045445 (2012).

[27] Z. Qiao, X. Li, W. K. Tse, H. Jiang, Y. Yao, and Q. Niu, Phys. Rev. B **87**, 125405 (2013).

[28] J. Wang, B. Lian, H. Zhang, Y. Xu, and S.-C. Zhang, Phys. Rev. Lett. **111**, 136801 (2013).

[29] C. Fang, M. J. Gilbert, and B. A. Bernevig, Phys. Rev. Lett. **112**, 046801 (2014).

[30] D. C. Elias, R. R. Nair, T. M. G. Mohiuddin, S. V. Morozov, P. Blake, M. P. Halsall, A. C. Ferrari, D. W. Boukhvalov, M. I. Katsnelson, A. K. Geim, and K. S. Novoselov, Science **323**, 610 (2009).

[31] J. Zhou, Q. Wang, Q. Sun, X. S. Chen, Y. Kawazoe, and P. Jena, Nano Lett. **9**, 3867 (2009).

[32] X. Q. Wang, H. D. Li, and J. T. Wang, Phys. Chem. Chem. Phys. **14**, 3031 (2012).

[33] F. Wang and Y. Ran, Phys. Rev. B **84**, 241103(R) (2011).

[34] A. Zhao and S. Q. Shen, Phys. Rev. B **85**, 085209 (2012).

[35] A. Mielke, J. Phys. A **24**, 3311 (1991).

[36] H. Tasaki, Prog. Theor. Phys. **99**, 489 (1998).

[37] E. H. Lieb, Phys. Rev. Lett. **62**, 1201 (1989).

[38] K. Sun, H. Yao, E. Fradkin, and S. A. Kivelson, Phys. Rev. Lett. **103**, 046811 (2009).

[39] T. Fukui, Y. Hatsugai, and H. Suzuki, J. Phys. Soc. Jpn. **74**, 1674 (2005); T. Fukui and Y. Hatsugai, *ibid.* **76**, 053702 (2007).

[40] B. L. Huang and C. Y. Mou, Europhys. Lett. **88**, 68005 (2009); B. L. Huang, M. C. Chang, and C. Y. Mou, Phys. Rev. B **82**, 155462 (2010).

[41] M. Auslendera and E. Kogan, Phys. A **302**, 345 (2001); Y. Motome and N. Furukawa, J. Phys. Chem. Solids **63**, 1357 (2002).

[42] S. T. Lee, S. M. Huang, and C. Y. Mou, arXiv:1308.4053.

[43] L. C. Lew, Yan Voon, E. Sandber, R. S. Aga, and A. A. Farajian, Appl. Phys. Lett. **97**, 163114 (2010).

[44] M. Houssa, E. Scalise, K. Sankaran, G. Pourtois, V. V. Afanas'ev, and A. Stesmans, Appl. Phys. Lett. **98**, 223107 (2011).

[45] P. Zhang, X. D. Li, C. H. Hu, S. Q. Wu, and Z. Z. Zhu, Phys. Lett. A **376**, 1230 (2012).

[46] J. Balakrishnan, G. Kok, Wai Koon, M. Jaiswal, A. H. Castro Neto, and B. Özyilmaz, Nat. Phys. **9**, 284 (2013).

[47] H. S. Liu, J. F. Gao, and J. J. Zhao, J. Phys. Chem. C **117**, 10353 (2013).

[48] The star of $\mathbf{k}$ here is the set of wave vectors which are obtained by threefold rotations of $\mathbf{k}$.